photonics

MDPI

Article

Multi-Spectral Quantum Cascade Lasers on Silicon With Integrated Multiplexers

Eric J. Stanton [1,*,†], Alexander Spott [1], Jon Peters [1], Michael L. Davenport [1], Aditya Malik [1], Nicolas Volet [1], Junqian Liu [1], Charles D. Merritt [2], Igor Vurgaftman [2], Chul Soo Kim [2], Jerry R. Meyer [2] and John E. Bowers [1]

1 Department of Electrical and Computer Engineering, University of California, Santa Barbara, CA 93106, USA; spott@ece.ucsb.edu (A.S.); peters@ece.ucsb.edu (J.P.); davenport.000@gmail.com (M.L.D.); amalik@ece.ucsb.edu (A.M.); nicolasvolet@hotmail.com (N.V.); junqian@ucsb.edu (J.L.); bowers@ece.ucsb.edu (J.E.B.)

2 Code 5613, Naval Research Laboratory, Washington, DC 20375, USA; Charles.Merritt@nrl.navy.mil (C.D.M.); igor.vurgaftman@nrl.navy.mil (I.V.); chulsoo.kim@nrl.navy.mil (C.S.K.); jerry.meyer@nrl.navy.mil (J.R.M.)

* Correspondence: eric.stanton@nist.gov

† Current address: Applied Physics Division, National Institute of Standards and Technology, Boulder, CO 80305, USA

Received: 3 January 2019; Accepted: 22 January 2019; Published: 24 January 2019

Abstract: Multi-spectral midwave-infrared (mid-IR) lasers are demonstrated by directly bonding quantum cascade epitaxial gain layers to silicon-on-insulator (SOI) waveguides with arrayed waveguide grating (AWG) multiplexers. Arrays of distributed feedback (DFB) and distributed Bragg-reflection (DBR) quantum cascade lasers (QCLs) emitting at ~4.7 µm wavelength are coupled to AWGs on the same chip. Low-loss spectral beam combining allows for brightness scaling by coupling the light generated by multiple input QCLs into the fundamental mode of a single output waveguide. Promising results are demonstrated and further improvements are in progress. This device can lead to compact and sensitive chemical detection systems using absorption spectroscopy across a broad spectral range in the mid-IR as well as a high-brightness multi-spectral source for power scaling.

Keywords: quantum cascade laser; silicon photonics; distributed feedback laser; mid-infrared; arrayed waveguide grating

1. Introduction

Compact, multi-spectral laser sources emitting in the midwave infrared (mid-IR) are in high demand for such applications as absorption spectroscopy in the molecular fingerprint region and infrared countermeasures against heat-seeking missiles [1–3]. Since a key practical requirement of these systems is that multiple mid-IR laser beams must be combined into a single output without sacrificing beam quality, research to develop this challenging capability has received high priority in recent years. Currently, the state-of-the-art for combining multiple quantum cascade laser (QCL) beams relies on external optics to provide multiplexing [4–7]. It has long been recognized, however, that it will be highly beneficial from the perspectives of system compactness and expense if multiple beams, in some cases spanning multiple spectral bands, can be combined efficiently before they leave the semiconductor chip. Several previous works have reported the use of Y-junctions to combine multiple QCL beams on the native indium phosphide (InP) substrate [8–10]. However, the Y-junction duplexer tree has inherently high loss [6], and integration on the native substrate precludes incorporating multiple gain materials on the same chip. One example of an integrated approach used an array of QCLs on InP coupled to an arrayed waveguide grating (AWG) on silicon germanium (SiGe) [7,11,12], though separate chips were necessary [13]. An attractive alternative is to integrate QCLs on silicon

(Si), which will allow the existing low-loss and large-scale fabrication infrastructure to be leveraged in the design of complex photonic integrated circuits (PICs) [14,15]. While others have developed QCL growth directly on Si, the laser performance reduced compared to lasers grown on a native substrate [16,17]. The heterogeneous platform is ideal for on-chip spectral beam combining to create high-brightness sources for the mid-IR [18,19], with the option of incorporating lasers emitting in other spectral bands, such as interband cascade lasers (ICLs) emitting between 3 and 4 µm [20], on the same chip. An important component of this platform is the arrayed waveguide grating, which has already been demonstrated using an off-chip source for multiplexing with low loss at 3.8 µm on the Si-on-insulator (SOI) platform [21]. Despite the increasing optical absorption in silica (SiO_2) with increasing wavelength, efficient low-loss AWGs on SOI are feasible up to ~5 µm, by increasing the Si waveguide thickness to reduce mode confinement in the SiO_2 [22]. In this work, we present the first demonstration of a multi-spectral QCL array on Si coupled to a single-output waveguide.

The recent development of QCLs integrated on Si substrates [14,15] shows that more complex PICs for the mid-IR will be possible by leveraging the Si photonic infrastructure. The present investigation aims to fabricate arrays of QCLs similar to those initially demonstrated, and combine the outputs from the individual lasers with an AWG integrated on the same chip. The laser mirrors are defined within the length of the active region with gratings etched in the top surface of the Si waveguides before bonding the gain material. Minor modifications of the laser design and processing protocol have been implemented to investigate their effects on the fabrication yield, thermal dissipation, and output power. The most significant modification is to employ an SOI waveguide platform rather than Si-on-nitride-on-insulator (SONOI) as in the previous demonstrations [14,15]. In that case the SONOI platform was chosen in order to establish an ultra-broadband platform supporting both SON waveguides for longer wavelengths and NOI waveguides for wavelengths as short as 300 nm [23–27]. Another recent study integrated QCLs on a Si-on-sapphire platform via transfer-printing [28], which enables low loss at longer wavelengths. However, at 4.7 µm the more standard SOI can still support low-loss waveguides. For applications focusing only on near- and mid-IR spectral regions (1.2–5.0 µm), SOI may be advantageous, since high-quality SOI is commercially available whereas SONOI is not. Furthermore, eliminating the Si_3N_4 layer lowers the thermal resistance between the devices and the heat sink below the substrate.

Cascaded stages of spectral beam combining, proceeding from dense to coarse wavelength combinations, have been proposed to create an ultra-broadband, multi-spectral high-brightness on-chip source [18,19]. The waveguide platform employed in the present mid-IR demonstration is quite suitable for bonding other laser gain materials that will expand the wavelength range. Previous AWGs have been reported in the mid-IR, besides the SOI AWG near 3.8 µm [21], including Ge-waveguide AWGs near 5 µm [29,30] and SiGe-waveguide AWGs at longer mid-IR wavelengths [7,31]. The AWG of the present work represents the longest operating wavelength, $\lambda = 4.7$ µm, to use the SOI platform. Recently, the wavelength range for low-loss waveguides on SOI has been extended by increasing the Si thickness as compared to conventional designs [22]. This technique has been used to support low-loss waveguides for the QCLs and AWG of the present work.

2. Design

The QCL structure was grown on an InP substrate by metal-organic chemical vapor deposition (MOCVD) at Thorlabs Quantum Electronics (TQE) and directly bonded to SOI with patterned waveguides. The material layers of the final QCL-on-SOI device are listed in Table 1. Figure 1a shows a schematic top-view of the QCL array and the AWG, and Figure 1b is a micrograph of a single 8-channel multi-spectral laser.

Table 1. Quantum cascade laser (QCL) layer structure.

Layer	Material	Thickness (nm)
Top contact	InP	1700
Top cladding	InP	2500
Active core	QC structure	1660
Bottom cladding	InP	113
Bottom contact	InP	230
Bonding super-lattice	InGaAs/InP	(9/9)×2
Bonding layer	InP	12
Waveguide core	Si	1500
Bottom cladding	SiO_2	1000
Substrate	Si	~720×10^3

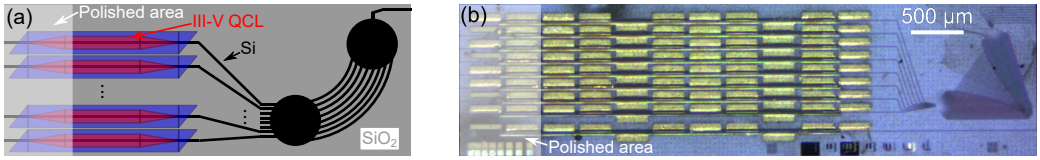

Figure 1. (**a**) Top-view schematic of the QCL array and arrayed waveguide grating (AWG). Mirrors are defined under the red III-V QCL ridges for both the distributed feedback (DFB) and distributed Bragg-reflection (DBR) type lasers. (**b**) Micrograph of a multi-spectral DFB laser, showing the individual lasers on the left and the AWG combiner on the right.

Each of the QCLs with 4 mm gain length has one of two types of gratings patterned into the underlying silicon waveguide: distributed feedback (DFB) gratings that extend throughout the laser cavity and distributed Bragg reflectors (DBR) that are patterned to provide reflection only at each end of the cavity. In general, it is expected that the DFB lasers are more likely to operate in a single longitudinal mode, while the DBR lasers should display higher efficiency. The application for the DFB lasers is focused on chemical detection by absorption spectroscopy since the output ideally has a single longitudinal mode, though it emits equally from the front and the back facets. The DBR lasers are designed to maximize emission through the AWG output for power scaling; however, these lasers have multiple longitudinal modes that may be undesirable for applications such as tunable laser spectroscopy. Each DFB laser has a quarter-wavelength ($\lambda/4$) phase shift section at the center of the gain region to promote lasing in a single longitudinal mode at the grating Bragg wavelength. Each DBR laser has a 1.0-mm-long grating as its back mirror and a 0.5-mm-long grating as its front mirror, which leaves a 2.5-mm-long section in the center with no grating. For each DFB and DBR array of eight lasers, the mean grating period is 744.0 nm and the pitch is 3.19 nm. This corresponds to a mean design wavelength of 4.630 µm (2160 cm^{-1}) and wavelength pitch of 20 nm (9 cm^{-1}).

The gratings are defined by etching a periodic rectangular pattern, with 23-nm depth, into the top of the Si waveguide before the gain material is bonded. For the DBR lasers, about six longitudinal modes exist in the 3-dB bandwidth of each mirror set. Our simulations project power reflections of 12% for the front mirrors and 93% for the back mirrors, corresponding to gratings strengths of $\kappa L = 1.2$ for the front mirror and $\kappa L = 2.5$ for the back mirror. The DFB lasers have a narrow lasing mode in the center of each stop-band, with a full width at half maximum (FWHM) of 8.0 MHz and a strong grating with $\kappa L = 9.9$. The III-V/Si tapers are similar to those used for the earlier QCLs on SONOI [14,15]. Since the taper design for the previous demonstrations on SONOI were functional, no attempt was made to improve the taper design here because the focus of this work is to demonstrate integration of the QCLs and AWG. While the intended function of the tapers is to efficiently couple light from the hybrid III-V/Si waveguide, where gain occurs, to the passive silicon waveguide, the results reported below are consistent with the earlier finding for QCLs integrated on silicon [14,15] that the tapers provided reflections, likely forming a secondary cavity for the DFB and DBR lasers.

This AWG, with the parameters listed in Table 2, is designed with the same methodology as in previous works at shorter wavelengths [32–34]. To our knowledge, this is the longest wavelength operation reported for an AWG on SOI. In part because of the long wavelength, a low-order grating of order 10 is produced. The channel spacing is chosen to include eight channels in the bandwidth limited by the QCL gain material. The AWG model predicts a total loss of 1.07 dB for the center channels, which is the sum of the side-order grating excitation of 0.63 dB, the arrayed waveguide aperture limitation of 0.09 dB, and a propagation loss of 0.35 dB. The peak transmission of the outer channels is 1.4-dB less than for the center channels. The channel spacing is ~20 nm (275 GHz) and the free spectral range (FSR) is 343 nm. The total footprint of an 8-channel QCL array and AWG is 6.0 mm^2.

Table 2. Design and layout dimensions for the AWG.

Number of channels	N_{ch}	8
Number of AWs	N_{AW}	73
Rowland radius	r	75.23 µm
AW length increment	ΔL	16.71 µm
AW width	w_{AW}	1.50 µm
AW width at FPR	$w_{AW\text{-}FPR}$	1.60 µm
i/o waveguide width	w_{io}	1.80 µm
i/o waveguide width at FPR	$w_{io\text{-}FPR}$	1.80 µm
AW pitch at FPR	$d_{c,AW}$	1.90 µm
i/o waveguide pitch at FPR	$d_{c,io}$	3.60 µm
Footprint area	S	3.68 mm^2

3. Methods

3.1. Fabrication

Figure 2 depicts the device fabrication process, which follows methods similar to our previous demonstrations of QCLs integrated on Si [14,15]. Here SOI replaces the SONOI waveguide platform. The reduced lower cladding thickness, where 1.0 µm of SiO_2 is used in place of 0.4 µm of SiN and 2.0 µm of SiO_2, is expected to improve the thermal conductivity from the III-V active region to the Si substrate. Figure 3 shows scanning electron micrographs (SEMs) of the AWG, the III-V mesa, and the grating etched in the top of the Si waveguide before the III-V material was bonded. This grating definition step corresponds to Figure 2a.

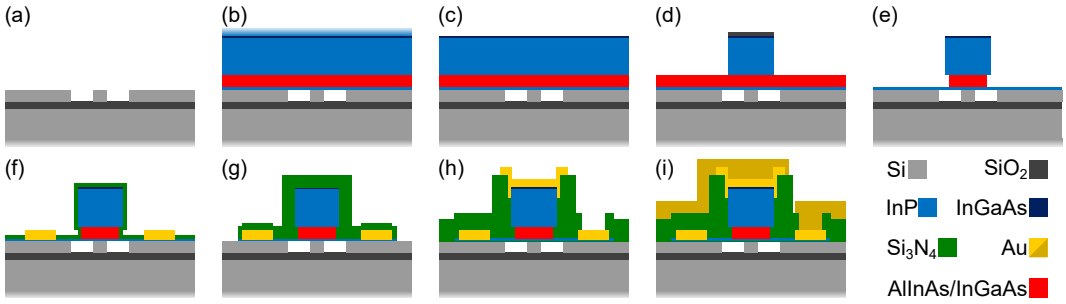

Figure 2. Processing steps: (**a**) gratings and Si waveguides are defined; (**b**) the QCL chip is bonded to the Si wafer; (**c**) the InP substrate is removed; (**d**) top contact and cladding layers are dry etched; (**e**) the active region is wet etched; (**f**) the bottom contact region is defined and gold is deposited; (**g**) Si_3N_4 is deposited and the bottom contact layer is etched; (**h**) vias are etched and the top contact metal is deposited; (**i**) probe metal is deposited.

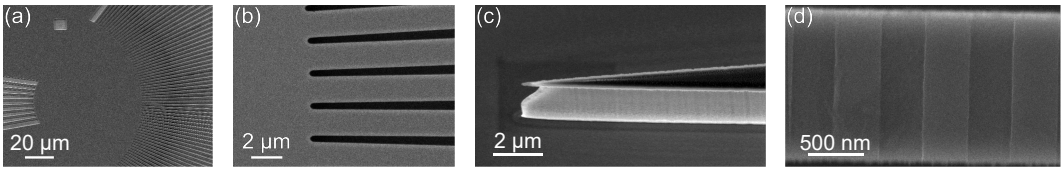

Figure 3. SEMs of the (**a**) star coupler of an AWG, (**b**) transition between the free-propagation region of the star coupler to the arrayed waveguides of an AWG, (**c**) slanted view of a QCL taper tip before etching the *n*-QC structure, where the top layer is the SiO_2 hardmask, and (**d**) a grating etched in the top of a Si waveguide before bonding the QCL.

3.2. Experimental Setups

Figure 4a–c provide schematics of the experimental setups for the AWG and QCL characterizations, while Figure 4d shows a photograph of the QCL LIV setup corresponding to the schematic in Figure 4b. The AWG transmission measurements were made using the setup in Figure 4a. A commercially available tunable QCL (TL) emits up to 400 mW continuous-wave (CW) in a free-space beam. The polarization controller (PC) consists of half-wave and quarter-wave plates. A parabolic mirror (Lens) couples the polarized beam into an angled-facet indium fluoride (InF) fiber. The other side of the fiber is polished with a flat facet and aligned to the input waveguide of an AWG test-chip. The output facet emits light into a similar fiber that couples to a HgCdTe detector (DET, Vigo PVI-4TE) whose temperature is regulated by a thermoelectric cooler (TEC). A second TEC is used with a thermistor and temperature control unit (Newport LDT-5500) to stabilize the AWG sample at room temperature.

Both QCL setups use the same pulsed current source (CS, Newport LDP-3830). Either one probe card, two probe cards, or individual probe needles are used to contact the probe pads on the lasers. The temperature of the copper stage is set within the range 18–60 °C. Figure 4b shows that a detector aligned to the laser output measures the light-current-voltage (LIV) characteristics. Two different detectors are used for either a large detection area or a high sensitivity. DET-A (Vigo PVI-4TE) is more sensitive, although its 1×1 mm^2 area does not capture all of the output light. DET-B (Vigo PVM-8), with a much larger 4×4 mm^2 detection area, is used to calibrate the output power by placing the detector very close to the laser output facet so as to assure capture of all the emitted power. The laser output spectra are measured with the setup shown in Figure 4c. An aspheric lens (Thorlabs 390037-E) collects the light and focuses it into a Fourier transform infrared (FTIR) spectrometer (Bruker Vertex 70) with a liquid nitrogen (LN) cooled HgCdTe detector.

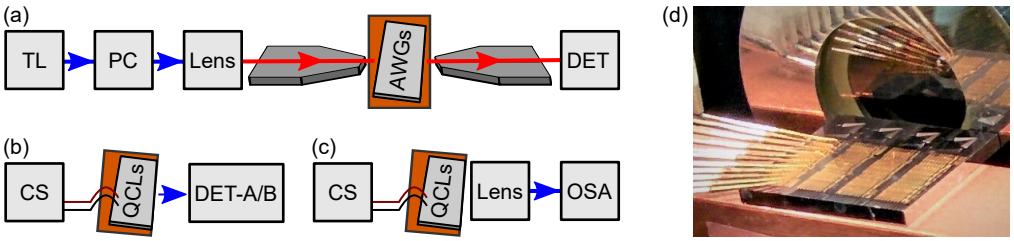

Figure 4. Experimental setups for (**a**) the AWG passive transmission, (**b**) the QCL LIV characteristics, and (**c**) the QCL spectral measurements. CS represents a current source and PC represents a polarization controller. (**d**) A photograph of the QCL array coupled to an AWG with the output collected by DET-A, corresponding to the schematic in (**b**).

4. Individual Laser Characteristics

Lasing is observed from 41 of the 132 fabricated devices, representing a yield of 28%. Of the failed devices, 37% were short-circuits, 54% were open-circuits, and 9% had typical laser I-V characteristics. None of the short- or open-circuited devices are considered in the following sections of this work. Each experimental investigation is performed on a different laser, so the data presented in each of the following sections come from separate devices.

Two fabrication issues in particular are thought to have contributed to the relatively low yield of functional devices compared to our previous investigations of QCLs integrated on Si [14,15]. First, the open-circuit behavior is likely caused by an insufficient etch down to the bottom contact layer, due to an etch-loading effect in the densely spaced lasers compared to the etch-monitor region. The second issue is that the nearly 6 µm topography from the QCL mesas a formed nonuniform photoresist thickness, resulting in short-circuits at the QCL taper tips during the contact-metal patterning steps. The first issue can be solved by forming an etch-monitor region with similarly dense spacing to the laser array, and the second issue can be solved by forming mesas in the QCL material near the lasers so the photoresist will planarize uniformly on the top surface of the InP. Similar issues were present in the previous fabrication of QCLs on SONOI, but the analysis was not affected since only individual lasers, rather than arrays, were studied.

The standard condition for testing the individual DFB and DBR lasers was an 800 mA current injection using 500 ns pulse lengths with 1% duty cycle, for which the bias was ∼14–16 V. Some devices were tested with up to 1.6 A drive current without damage. However, others damaged at 1.0 A, so the subsequent tests were limited to 800 mA to preserve the lasers. The maximum emitted powers were 1.4 mW from a DFB laser and 2.5 mW from a DBR laser. In general, the *L-I* curves for DFB lasers had a single linear slope, while those for DBR lasers showed multiple linear slopes. This is likely due to the multiple modes of the DBR lasers, which can be selected preferentially as increasing current alters the carrier dynamics and heats the gain material. Both laser types exhibit a roll-over in the output power at high current injection (typically above 600 mA) due to the increased carrier concentration in the active region. The slope efficiency for the DFB lasers is about 2.4%, which is limited by the extraction efficiency through the III-V/Si taper.

4.1. Temperature and Pulse Width Dependence

Figure 5 shows representative pulsed LIV characteristics of DFB and DBR lasers at a series of temperatures in the range 20–60 °C. The threshold currents and slope efficiencies were determined from linear fits to the output power in the first 50 mA above the estimated thresholds. Trends of increasing threshold current and decreasing slope efficiency with temperature are observed, as expected, although at a slow rate.

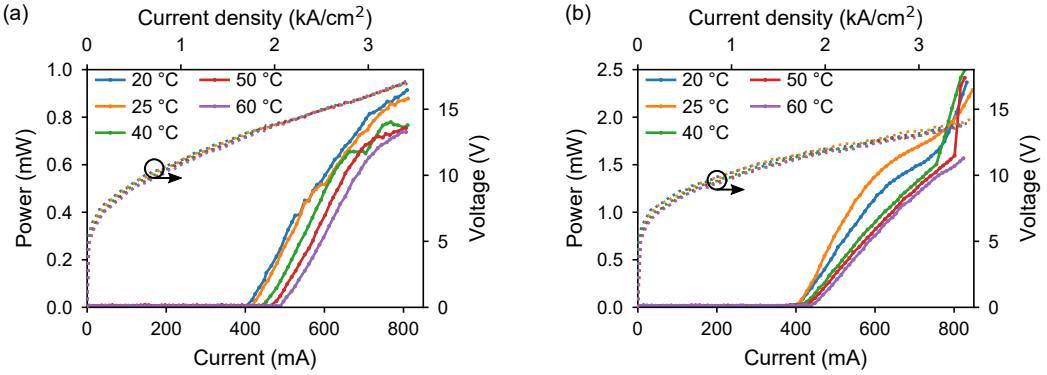

Figure 5. Light-current-voltage (LIV) dependence on temperature for (**a**) DFB and (**b**) DBR devices.

Figure 6 plots the extracted threshold current densities (J_{th}) and slope efficiencies (η_d), along with fits to the exponential relations [35]: $J_{th} = J_0 e^{T/T_0}$ and $\eta_d = \eta_1 e^{-T/T_1}$. For the DFB laser these fits extract $T_0 = 218 \pm 4$ K and $T_1 = 221 \pm 8$ K, while fits for the DBR laser result in $T_0 = 423 \pm 34$ K and $T_1 = 178 \pm 45$ K. The $\pm$ uncertainty values represent the 34.1% confidence intervals. The differences between the DFB and DBR laser characteristics are probably not directly attributable to the mirror properties, but rather to variations in the fabrication and the multi-longitudinal mode operation of the DBR lasers. Note also that the much larger characteristic temperatures of the DBR laser are likely due in part to the different selection of longitudinal or lateral modes that lase at different temperatures.

Thus, while the T_0 and T_1 values for DBR lasers should nominally be similar to those of the DFB lasers, the method used here to determine the characteristic temperatures is less reliable for the DBR lasers. For comparison, the corresponding values from our previous demonstration of DFB QCLs on SONOI [15], which employed 3-mm gain lengths, were $T_0 = 199$ K and $T_1 = 222$ K.

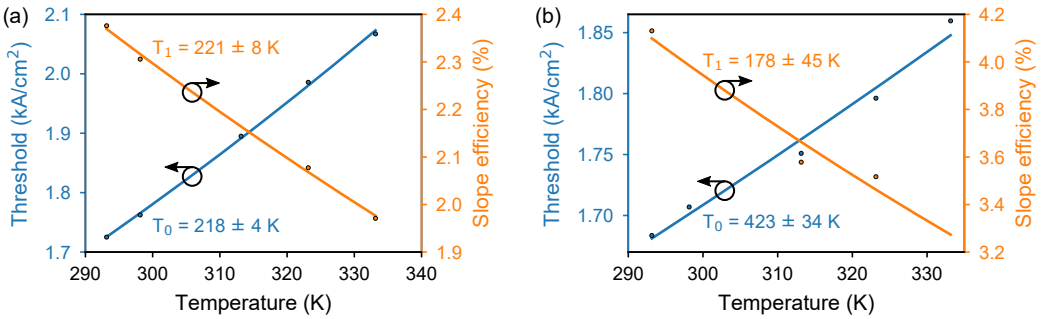

Figure 6. Current density at threshold (in orange) and slope efficiency (in blue) extracted as a function of temperature for (**a**) DFB and (**b**) DBR lasers.

Figure 7 shows the output spectra of (a) the DFB and (b) the DBR lasers at a series of temperatures between 20 and 60 °C. The DFB and DBR lasers are driven with 200 ns and 100 ns pulse widths, respectively, at an 800-mA level. The temperature dependences of the peak wavelengths yield linear temperature tuning coefficients of ∼270 pm/K and ∼300 pm/K, respectively. The temperature-induced shift in wavelength for the AWG channels is predominantly incurred by the thermo-optic effect in Si, which is also the case for the temperature tuning of the lasers. Simulations predict a wavelength tuning for the AWG channels of ∼290 pm/K, which is similar to these experimental measurements of the laser tuning.

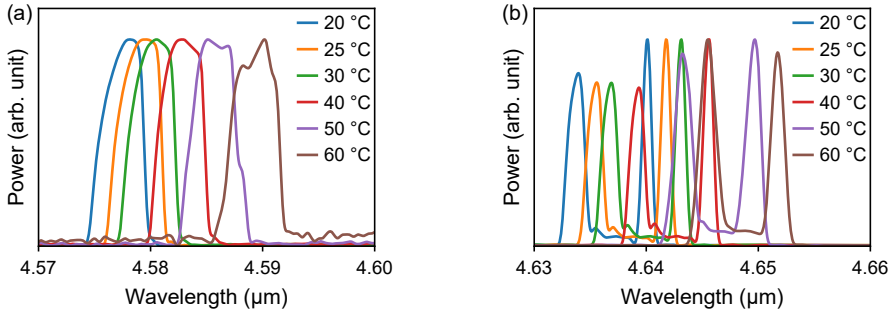

Figure 7. Normalized spectral dependence on the temperature for (**a**) a DFB laser from channel 2 with a 200 ns drive pulse width and (**b**) a DBR laser from channel 5 with a 100 ns drive pulse width. Heating during the pulse limits the linewidth of each mode.

None of the devices were lased under CW injection conditions. However, up to a 5% duty cycle, the output power does not degrade due to heating. The LIV and spectral characteristics were measured at 20 °C as a function of pulsing duty cycle, up to the maximum value 5.0% that was limited by the driver. The temperature-induced evolution of the mode preference has more effect on the output power than the increase of temperature with duty cycle. We note that under the same pulsing conditions, the previous QCLs on SONOI [15] showed a much more pronounced decrease of output power with duty cycle, which may be attributed to the lower thermal resistance of this SOI platform with a decreased low cladding thickness relative to the previously-used SONOI platform.

With a fixed pulse period of 50 µs, we also measured the emission spectra at a series of pulse widths varying from 50 ns to 1.0 µs. Whereas the spectral linewidths for both types of lasers were <2 nm at the shortest pulse width, they broadened to as much as 18 nm for the longest pulse. This broadening is attributable to temperature chirp, which may be expected to alter the mode preferences as the pulse

progresses. In addition to the broadening, the centroid wavelengths became longer with increasing pulse length, due to heating.

4.2. Effect of Removing One III-V/Si Taper

To investigate the effectiveness of the III-V/Si taper, one DFB chip was polished through the taper transition to leave a hybrid III-V/Si waveguide at the back facet. The polished area is indicated in Figure 1 with a white-shaded region on the left side of the QCL array, and two lasers from this chip were characterized. Figure 8 plots the LIV and spectral characteristics measured for the two devices before and after one taper was removed from each laser. The maximum powers emitted from the hybrid III-V/Si facets were 35 mW and 83 mW at 890 mA and 866 mA, respectively, which compares to the output powers of 2.5 mW and 0.16 mW (at 812 mA and 804 mA) before the tapers were polished off. That is, the outputs increased by factors of 33 and 219. The threshold current for the first laser was within the measurement tolerance compared to before the taper was polished, while that of the second laser increased by 24%. The increase could be associated with a variation of the mode preference, or simply because the taper had induced more reflection (to provide a lower-loss cavity) than the hybrid III-V/Si facet that replaced it. The centroid wavelength for the first laser did not shift although the line broadened considerably, whereas the second laser red-shifted by about 6 nm following removal of the taper. Again, these observations are most likely dominated by variations of the mode preferences.

Similar dramatic increases of the output power after one of the tapers is polished away were observed previously in the studies of Fabry-Perot and DFB QCLs integrated on the SONOI platform [14,15]. These observations indicate that improving the III-V/Si taper transmission would greatly increase the output power. While the threshold tends not to vary substantially when a taper is removed, the efficiency increases dramatically after removing the taper.

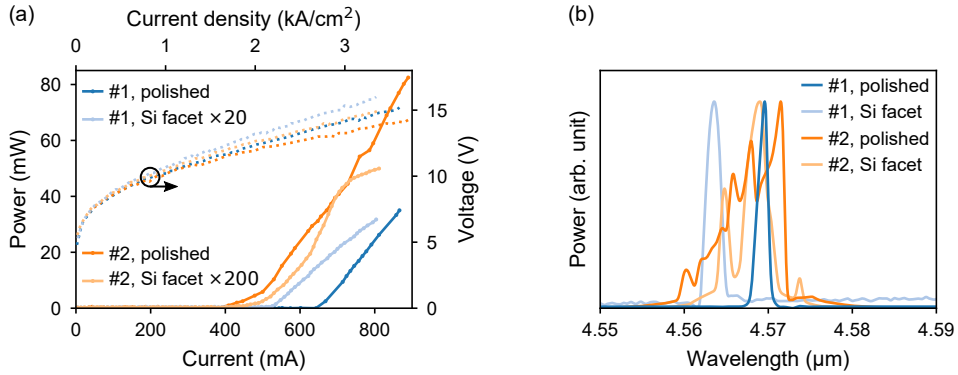

Figure 8. (**a**) LIV and (**b**) spectral characteristics of two DFB lasers, corresponding to emission from the hybrid III-V/Si facet after one taper was polished off.

5. Beam Combining with AWGs

5.1. AWGs

The AWG transmission characteristics were first measured on a dedicated test-chip that was fabricated separately without integrated QCL arrays. The curves in Figure 9 show the simulated TM-mode transmission spectra of the AWG design with eight channels, which agree well with the measured transmission data points. The center wavelength for the test AWGs is 4.70 μm, while the AWGs integrated with the QCLs are centered at 4.63 μm due to a slight variation of the waveguide widths. The multi-spectral QCLs may have reduced output from the AWG due to mis-alignment of the QCL and AWG channels.

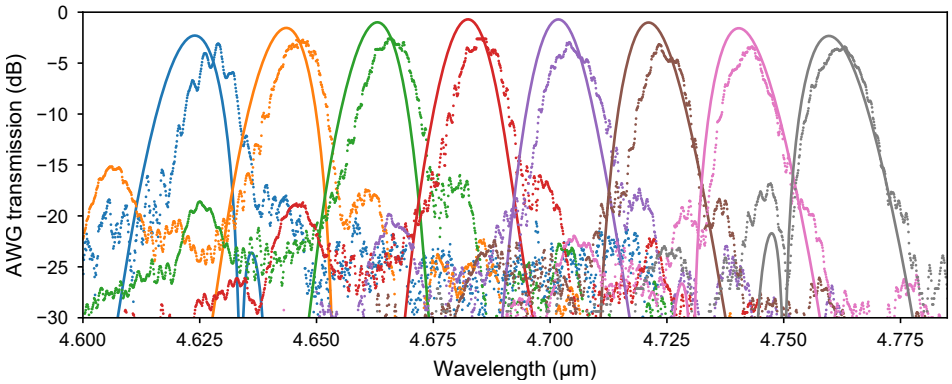

Figure 9. Transmission spectra for a similar AWG, fabricated separately from the QCL array. The solid curves are simulated and the points are measured data.

5.2. Multi-Spectral Lasers

Measurements of the power emitted from AWG output waveguides have confirmed spectral beam combining of multiple QCLs in arrays of lasers. The emitted power scales with the number of lasers operated simultaneously. Because of the relatively low yield in processing the present DFB and DBR lasers coupled to AWGs, at most three lasers per bar were operational. In addition, the channels available for characterization are limited by the device yield. The multi-spectral lasers reported in this section are separate devices from the individual lasers reported in the previous section. For each functioning multi-spectral laser, LIVs and spectra were measured from the front output, through the AWG. The LIV characteristics were acquired for all permutations of driving 1, 2, or 3 lasers simultaneously, while the spectra were measured at drive currents of 800 mA per laser. All of the reported LIV and spectral measurements were acquired at a pulse width of 500 ns. Figure 10a shows the LIV characteristics of a multi-spectral 3-channel DFB bar, while Figure 11a shows the analogous data for a 2-channel DBR bar. In Figures 10b and 11b the spectra of two DFB and two DBR lasers are shown, respectively. The individual lasers are identified by the channel numbers feeding into the AWG (e.g., channels 3, 5, and 6 in the case of Figure 10a are found in Figure 10b). These measurements require two probe cards and a set of four individual probes to drive all the lasers at once. The LIV plot is given as a function of drive current per laser, assuming that the net drive current is split equally among the lasers. This is not strictly correct, however, since each laser has a slightly different series resistance (thus it is more accurate to say that the current scale in Figure 10a is total drive current divided by the number of lasers driven by the current).

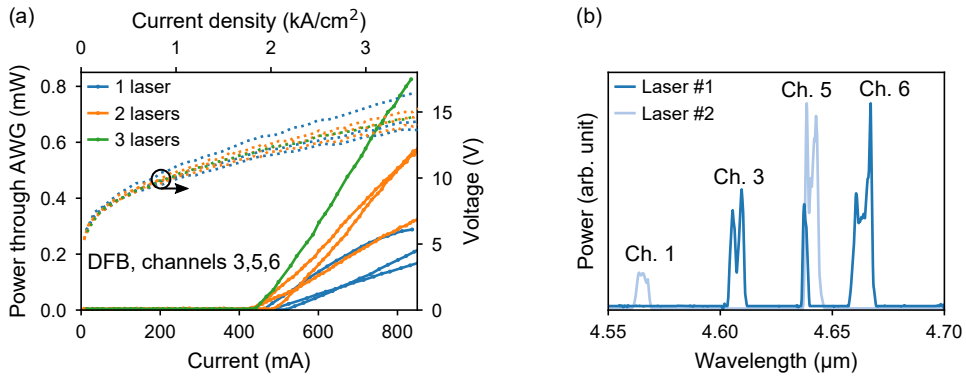

Figure 10. (**a**) LIV plots of a multi-spectral three-channel DFB while driving laser channels 3, 5, and 6. (**b**) Spectra of the three-channel DFB laser (Laser #1) and another two-channel DFB laser (Laser #2).

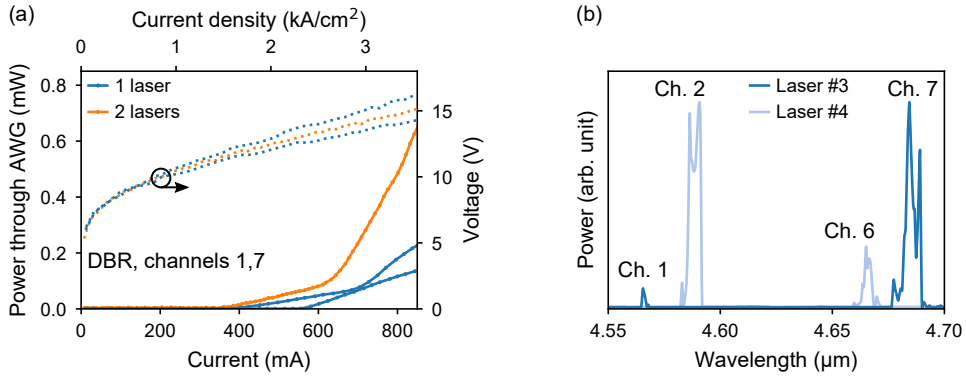

Figure 11. (**a**) LIV plots of a multi-spectral two-channel DBR while driving laser channels 1 and 7. (**b**) Spectra of the two-channel DBR laser (Laser #3) and another two-channel DFB laser (Laser #4).

A key concern about driving multiple lasers at once is that heating or some other cross-talk mechanism can degrade the total output power when all are driven simultaneously, as compared to the sum when each laser is driven individually. This figure-of-merit, termed here as the "power degradation" (D), is calculated for a pair of lasers (labeled 1 and 2) as:

$$D = 10 \log_{10} \frac{P_{1\&2,\max}}{P_{1,\max} + P_{2,\max}}. \quad (1)$$

Figure 12 plots this power degradation parameter for multiple pairs of lasers coupled through the AWG, as a function of distance between the pair of lasers. If thermal crosstalk was responsible for the degradation, then D should become more negative with decreasing distance between the lasers. This trend is not evident, however, so any degradation appears to arise from other effects. A probable contributor to the variation in D is that each laser has a different series resistance. Since only one current source is used, each laser does not have the same drive current due to the different resistance. The figure also indicates that D is nearly as likely to be positive as negative, which means that in some cases the net power increases rather than decreases when multiple devices are operated at once. However, the observed variations in D are likely caused by a variation in individual laser drive current while lasers are driven simultaneously due to unequal laser series resistances, as shown in Figure 10a and Figure 11a. We expect D to drastically decrease when individual current drivers are used for each laser.

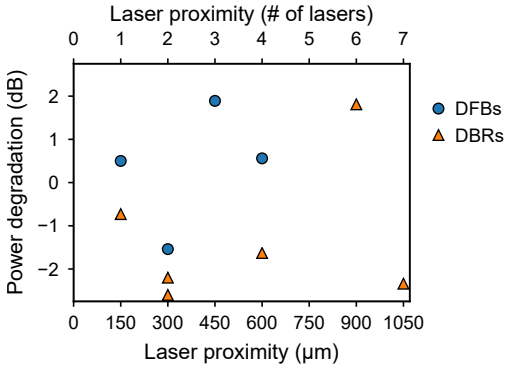

Figure 12. Power degradation dependence on proximity for multiple pairs of lasers.

6. Conclusions

We have demonstrated multi-spectral QCLs on an SOI platform by spectrally combining beams from multiple lasers with AWGs. The data presented confirm the combination of three functioning devices from an array of DFB lasers and two functioning devices from an array of DBR lasers. Analysis of individual lasers indicates an improved thermal performance compared to our previous work,

with the output power not degrading with at least 5% duty cycle pulses. In future work, achieving CW operation at room temperature would require a reduced thermal impedance from the III-V gain region to the heat sink. One option is to flip-chip bond the lasers to a submount. In addition, reducing the III-V/Si taper transition loss and increasing the coupling efficiency at the tapers will dramatically increase the fraction of generated light that is transferred to the passive Si waveguide, and correspondingly the net output power in the combined beam. A modified fabrication process is proposed to address the taper transition issue that prevented detailed analysis of the taper design. While a small fraction of the light generated by the QCLs actually reached the AWGs in the present experiments, it is encouraging that the AWGs combined the available beams quite efficiently. SOI is typically avoided in this spectral region due to the SiO_2 absorption, so this is the longest operation wavelength for an AWG using SOI waveguides. Since this is the first PIC with integrated QCLs combined into a common output on a Si substrate, its demonstration marks an important step towards large-scale, low-cost, and high-performance mid-IR photonic devices.

Author Contributions: Conceptualization, E.J.S.; Data curation, E.J.S.; Formal analysis, E.J.S.; Investigation, E.J.S., A.S., J.P., A.M. and J.L.; Methodology, E.J.S., A.S., M.L.D. and N.V.; Project administration, J.R.M. and J.E.B.; Supervision, C.D.M., I.V., C.S.K., J.R.M. and J.E.B.; Visualization, E.J.S.; Writing—original draft, E.J.S.; Writing—review & editing, E.J.S., A.S., N.V., J.R.M. and J.E.B.

Funding: This research was funded by the Air Force Research Laboratory (AFRL) grant number FA8650-17-C-5402 and the Office of Naval Research (ONR). N.V. acknowledges support from the Swiss National Science Foundation.

Acknowledgments: The authors thank the UCSB Nanofabrication Facility for technical support.

Conflicts of Interest: The authors declare no conflict of interest.

References

1. Day, T.; Pushkarsky, M.; Caffey, D.; Cecchetti, K.; Arp, R.; Whitmore, A.; Henson, M.; Takeuchi, E.B. Quantum cascade lasers for defense and security. *Proc. SPIE* **2013**, *8898*, 889802.
2. Razeghi, M.; Lu, Q.; Bandyopadhyay, N.; Zhou, W.; Heydari, D.; Bai, Y.; Slivken, S. Quantum cascade lasers: from tool to product. *Opt. Express* **2015**, *23*, 8462–8475. [CrossRef] [PubMed]
3. Vitiello, M.S.; Scalari, G.; Williams, B.; De Natale, P. Quantum cascade lasers: 20 years of challenges. *Opt. Express* **2015**, *23*, 5167–5182. [CrossRef] [PubMed]
4. Lee, B.G.; Kansky, J.; Goyal, A.K.; Pflügl, C.; Diehl, L.; Belkin, M.A.; Sanchez, A.; Capasso, F.A. Beam combining of quantum cascade laser arrays. *Opt. Express* **2009**, *17*, 16216–16224. [CrossRef] [PubMed]
5. Rauter, P.; Capasso, F. Multi-wavelength quantum cascade laser arrays. *Laser Photonics Rev.* **2015**, *9*, 452–477. [CrossRef]
6. Huang, R.K.; Chann, B.; Burgess, J.; Lochman, B.; Zhou, W.; Cruz, M.; Cook, R.; Dugmore, D.; Shattuck, J.; Tayebati, P. Teradiode's high brightness semiconductor lasers. In Proceedings of the Components and Packaging for Laser Systems II, San Francisco, CA, USA, 16–18 February 2016; Voume 9730, p. 0C.
7. Koshkinbayeva, A.; Barritault, P.; Ortiz, S.; Boutami, S.; Brun, M.; Hartmann, J.M.; Brianceau, P.; Lartigue, O.; Boulila, F.; Orobtchouk, R.; et al. Impact of Non-Central Input in $N \times M$ Mid-IR Arrayed Waveguide Gratings Integrated on Si. *IEEE Photonics Technol. Lett.* **2016**, *28*, 2191–2194. [CrossRef]
8. Hoffmann, L.K.; Klinkmüller, M.; Mujagić, E.; Semtsiv, M.P.; Schrenk, W.; Masselink, W.T.; Strasser, G. Tree array quantum cascade laser. *Opt. Express* **2009**, *17*, 649–657. [CrossRef] [PubMed]
9. Lyakh, A.; Maulini, R.; Tsekoun, A.; Go, R.; Patel, C.K.N. Continuous wave operation of buried heterostructure 4.6 µm quantum cascade laser Y-junctions and tree arrays. *Opt. Express* **2014**, *22*, 1203–1208. [CrossRef] [PubMed]
10. Zhou, W.; Wu, D.; McClintock, R.; Slivken, S.; Razeghi, M. High performance monolithic, broadly tunable mid-infrared quantum cascade lasers. *Optica* **2017**, *4*, 1228–1231. [CrossRef]
11. Labeye, P.; Koshkinbayeva, A.; Dupoy, M.; Barritault, P.; Lartigue, O.; Fournier, M.; Fedeli, J.; Garcia, S.; Nicoletti, S.; Duraffourg, L. Multiplexing photonic devices integrated on a silicon/germanium platform for mid-infrared gas sensing. In Proceedings of the 2017 Conference on Lasers and Electro-Optics Europe European Quantum Electronics Conference (CLEO/Europe-EQEC), Munich, Germany, 25–29 June 2017.

12. Labeye, P.; Koshkinbayeva, A.; Dupoy, M.; Barritault, P.; Lartigue, O.; Fournier, M.; Fedeli, J.M.; Boutami, S.; Garcia, S.; Nicoletti, S.; et al. Multiplexing photonic devices integrated on a silicon/germanium platform for the mid-infrared. In *Integrated Optics: Devices, Materials, and Technologies XXI*; SPIE: Bellingham, WA, USA, 2017; Volume 10106, p. 101060Y.
13. Bizet, L.; Vallon, R.; Parvitte, B.; Brun, M.; Maisons, G.; Carras, M.; Zeninari, V. Multi-gas sensing with quantum cascade laser array in the mid-infrared region. *Appl. Phys. B* **2017**, *123*, 145. [CrossRef]
14. Spott, A.; Peters, J.; Davenport, M.L.; Stanton, E.J.; Merritt, C.D.; Bewley, W.W.; Vurgaftman, I.; Kim, C.S.; Meyer, J.R.; Kirch, J.; et al. Quantum cascade laser on silicon. *Optica* **2016**, *3*, 545–551. [CrossRef]
15. Spott, A.; Peters, J.; Davenport, M.L.; Stanton, E.J.; Zhang, C.; Merritt, C.D.; Bewley, W.W.; Vurgaftman, I.; Kim, C.S.; Meyer, J.R.; et al. Heterogeneously Integrated Distributed Feedback Quantum Cascade Lasers on Silicon. *Photonics* **2016**, *3*, 35. [CrossRef]
16. Go, R.; Krysiak, H.; Fetters, M.; Figueiredo, P.; Suttinger, M.; Fang, X.M.; Eisenbach, A.; Fastenau, J.M.; Lubyshev, D.; Liu, A.W.K.; et al. InP-based quantum cascade lasers monolithically integrated onto silicon. *Opt. Express* **2018**, *26*, 22389–22393. [CrossRef] [PubMed]
17. Nguyen-Van, H.; Baranov, A.N.; Loghmari, Z.; Cerutti, L.; Rodriguez, J.B.; Tournet, J.; Narcy, G.; Boissier, G.; Patriarche, G.; Bahriz, M.; et al. Quantum cascade lasers grown on silicon. *Sci. Rep.* **2018**, *8*, 7206. [CrossRef] [PubMed]
18. Stanton, E.J.; Heck, M.J.; Bovington, J.; Spott, A.; Bowers, J.E. Multi-octave spectral beam combiner on ultra-broadband photonic integrated circuit platform. *Opt. Express* **2015**, *23*, 11272–11283. [CrossRef] [PubMed]
19. Spott, A.; Stanton, E.J.; Volet, N.; Peters, J.D.; Meyer, J.R.; Bowers, J.E. Heterogeneous Integration for Mid-Infrared Silicon Photonics. *IEEE J. Sel. Top. Quantum Electron.* **2017**, *23*, 8200810. [CrossRef]
20. Spott, A.; Stanton, E.J.; Torres, A.; Davenport, M.L.; Canedy, C.L.; Vurgaftman, I.; Kim, M.; Kim, C.S.; Merritt, C.D.; Bewley, W.W.; et al. Interband cascade laser on silicon. *Optica* **2018**, *5*, 996–1005. [CrossRef]
21. Muneeb, M.; Chen, X.; Verheyen, P.; Lepage, G.; Pathak, S.; Ryckeboer, E.; Malik, A.; Kuyken, B.; Nedeljkovic, M.; Van Campenhout, J.; et al. Demonstration of Silicon-on-insulator mid-infrared spectrometers operating at 3.8 µm. *Opt. Express* **2013**, *21*, 11659–11669. [CrossRef]
22. Miller, S.A.; Yu, M.; Ji, X.; Griffith, A.G.; Cardenas, J.; Gaeta, A.L.; Lipson, M. Low-loss silicon platform for broadband mid-infrared photonics. *Optica* **2017**, *4*, 707–712. [CrossRef]
23. Keck, D.B.; Maurer, R.D.; Schultz, P.C. On the ultimate lower limit of attenuation in glass optical waveguides. *Appl. Phys. Lett.* **1973**, *22*, 307–309. [CrossRef]
24. Izawa, T.; Shibata, N.; Takeda, A. Optical attenuation in pure and doped fused silica in the IR wavelength region. *Appl. Phys. Lett.* **1977**, *31*, 33–35. [CrossRef]
25. Philipp, H.R. Optical properties of silicon nitride. *J. Electrochem. Soc.* **1973**, *120*, 295–300. [CrossRef]
26. Lin, P.T.; Singh, V.; Lin, H.Y.G.; Tiwald, T.; Kimerling, L.C.; Agarwal, A.M. Low-Stress Silicon Nitride Platform for Mid-Infrared Broadband and Monolithically Integrated Microphotonics. *Adv. Opt. Mater.* **2013**, *1*, 732–739. [CrossRef]
27. Tai Lin, P.; Singh, V.; Kimerling, L.; Murthy Agarwal, A. Planar silicon nitride mid-infrared devices. *Appl. Phys. Lett.* **2013**, *102*, 251121. [CrossRef]
28. Jung, S.; Kirch, J.; Kim, J.H.; Mawst, L.J.; Botez, D.; Belkin, M.A. Quantum cascade lasers transfer-printed on silicon-on-sapphire. *Appl. Phys. Lett.* **2017**, *111*, 211102. [CrossRef]
29. Malik, A.; Muneeb, M.; Pathak, S.; Shimura, Y.; Van Campenhout, J.; Loo, R.; Roelkens, G. Germanium-on-Silicon Mid-Infrared Arrayed Waveguide Grating Multiplexers. *IEEE Photonics Technol. Lett.* **2013**, *25*, 1805–1808. [CrossRef]
30. Malik, A.; Stanton, E.J.; Liu, J.; Spott, A.; Bowers, J.E. High Performance 7 × 8 Ge-on-Si Arrayed Waveguide Gratings for the Midinfrared. *IEEE J. Sel. Top. Quantum Electron.* **2018**, *24*, 1–8. [CrossRef]
31. Fedeli, J.M.; Nicoletti, S. Mid-infrared (Mid-IR) silicon-based photonics. *Proc. IEEE* **2018**, *106*, 2302–2312 [CrossRef]
32. Stanton, E.J.; Spott, A.; Davenport, M.L.; Volet, N.; Bowers, J.E. Low-loss arrayed waveguide grating at 760 nm. *Opt. Lett.* **2016**, *41*, 1785–1788. [CrossRef]
33. Stanton, E.J.; Volet, N.; Bowers, J.E. Low-loss demonstration and refined characterization of silicon arrayed waveguide gratings in the near-infrared. *Opt. Express* **2017**, *25*, 30651–30663. [CrossRef]

34. Stanton, E.J.; Volet, N.; Bowers, J.E. Silicon arrayed waveguide gratings at 2.0-µm wavelength characterized with an on-chip resonator. *Opt. Lett.* **2018**, *43*, 1135–1138. [CrossRef] [PubMed]
35. Pankove, J. Temperature dependence of emission efficiency and lasing threshold in laser diodes. *IEEE J. Quantum Electron.* **1968**, *4*, 119–122. [CrossRef]